https://doi.org/10.5194/essd-2026-295
Preprint. Discussion started: 23 June 2026

Open Access Earth System Science Data Discussions

A 600-year gridded temperature dataset for East Asia based on Analogue Method

Xiaoyue Yan[1], Xuezhen Zhang[2,3], Linhao Zhong[1]

[1]National Institute of Natural Hazards, Ministry of Emergency Management of China, Beijing, 100085, China
[2]Institute of Geographical Sciences and Natural Resources Research, Chinese Academy of Sciences (CAS), Beijing, 100101, China
[3]College of Resources and Environment, University of Chinese Academy of Sciences, Beijing, 100049, China

Correspondence to: Xuezhen Zhang (xzzhang@igsnrr.ac.cn)

Abstract. Long-term gridded climate datasets are essential for for investigating the spatiotemporal variability and trends of regional climate. Developing reliable gridded reconstructions for the past few centuries requires preserving the spatial co-variability of climate variables while maintaining reconstruction efficiency. This study develops a gridded temperature dataset for East Asia (EA) spanning 1400-2000 CE, reconstructed using an improved Analogue Method (AM) based on climate proxy records and model simulations, at annual temporal resolution and $1° \times 1°$ spatial resolution. During the overlapping period of 1901-2000, the reconstructed mean temperature series is strongly correlated with instrumental observations ($r=0.74$, $p<0.01$). In addition, the leading empirical orthogonal function (EOF1) mode of the reconstruction is highly consistent with that derived from instrumental observations, indicating that the reconstruction captures the dominant mode of temperature variation over EA. The reconstruction further shows that thetemperature variations over the past 600 years can be divided into three phases: a cooling phase (1400-1510), a fluctuating cold phase (1511-1844), and a warming phase (1845-2000). The most rapid centennial-scale cooling and warming occurred during 1400-1500 (-0.31 °C/100 a) and 1900-2000 (0.58 °C/100 a), respectively. Spatially, temperature variability is strongest in the core region of the Siberian High. This dataset a valuable basis for understanding historical temperature variability and associated heat and cold extremes in EA, and for further examining long-term regional climate change. The dataset can open access on https://doi.org/10.5281/zenodo.18477496 (Yan et al, 2026).

1 Introduction

Climate change and variability operate across multiple timescales. Over the past millennium, climate variations were dominated primarily by natural forcing during the preindustrial period, but have become increasingly influenced by anthropogenic forcing since the Industrial Revolution (IPCC, 2022; Wang et al., 2023; Wang et al., 2020). Temperature is one of the most direct and sensitive indicators of this transition. As anthropogenic forcing has intensified, global temperatures have risen rapidly, posing major challenges to ecosystems, human health, and socio-economic systems (IPCC,

https://doi.org/10.5194/essd-2026-295
Preprint. Discussion started: 23 June 2026

2022). However, decadal-scale fluctuations have remained superimposed on the long-term warming trend. For example, a warming hiatus, or global warming slowdown, was observed during 1995-2012, when the warming rate was only 0.05 °C/10 a, compared with 0.18 °C/10 a during 1970-1998 (Medhaug et al., 2017; Zhang et al., 2016; Karl et al., 2015). It remains unclear whether this hiatus was driven primarily by internal climate variability or external forcing, because the relatively short instrumental record makes it difficult to distinguish internal variability from externally forced change (Medhaug et al., 2017). Therefore, recent temperature variations need to be evaluated in a historical context using long-term, high-resolution temperature datasets.

East Asia (EA), characterized by a complex monsoon-dominated climate system, exhibits substantial temperature variation across multiple timescales and is therefore a key region for climate change research (Gong et al., 2022; Cao et al., 2021; Hua et al., 2021). Although a few station records in EA extend back to the late 19th century, spatially extensive instrumental observations across the region did not become available until the 1950s (Ren et al., 2021; Cao et al., 2013). The limited length and spatial coverage of instrumental records make it difficult to assess temperature variation on decadal to centennial timescales. However, EA offers a unique opportunity to overcome this limitation, as its extensive paleoclimate archives (e.g., tree rings, glacier ice, corals, and historical documents) provide a strong foundation for long-term temperature reconstructions (Anderson et al., 2019; Chen et al., 2018). Consequently, the scientific importance of East Asia, coupled with the abundance of proxy records, makes the region particularly suitable for developing long-term, high-resolution gridded temperature datasets.

Recent proxy-based studies have reconstructed gridded temperature fields across Asia, particularly in EA, covering the past several centuries to millennia, thereby advancing our understanding of regional-scale temperature variation (Zhang et al., 2018; Shi et al., 2015). However, these reconstructions still have significant limitations. For instance, most datasets have relatively coarse spatial resolutions, typically around 5° × 5° (Zhang et al., 2018; Cook et al., 2013). Furthermore, many proxy-based reconstructions tend to underestimate the amplitude of temperature variability, particularly at low-frequency and multidecadal scales, a well-known "loss-of-variance" problem (Christiansen and Ljungqvist, 2017; von Storch et al., 2004). This issue can introduce uncertainties, especially when proxy networks are noisy or geographically sparse, reducing the reliability of climate inferences for earlier centuries (Anchukaitis and Smerdon, 2022; Christiansen and Ljungqvist, 2017).

The shortcomings of existing datasets are partly rooted in the reconstruction methodologies used. Traditional statistical climate field reconstruction (CFR) approaches, such as Point-by-Point Regression (PPR), rely on spatial covariance relationships calibrated using modern instrumental records (Freund et al., 2023; Yun et al., 2021; Smerdon et al., 2010; Luterbacher et al., 2007; Cook et al., 2004, 2002). However, the assumed stationarity of these relationships may not remain valid under climate boundary conditions different from those of the instrumental period. Climate model simulations provide dynamically consistent temperature fields (Deser et al., 2020), but their ability to reproduce historical temperature variability is limited by uncertainties in external forcings, model parameterizations, and climate variability (Jain et al., 2023; Jansson et al., 2021). Paleoclimate Data Assimilation (PDA) integrates proxy records with model simulations through observation

https://doi.org/10.5194/essd-2026-295
Preprint. Discussion started: 23 June 2026

operators in an assimilation framework, hence producing physically consistent reconstructions constrained by proxy evidence (Zhang et al, 2025a; Hakim, et al., 2016; Steiger et al., 2014; Bhend et al., 2012; von Storch et al., 2000). Nevertheless, its widespread adoption is constrained by high computational costs, and reliance on a single-model framework can introduce additional uncertainties (Steiger et al., 2014).

An ideal gridded climate reconstruction approach should satisfy two key requirements: (1) accurately represent historical climate states while preserving physically consistent spatial relationships, and (2) achieve high computational efficiency. Among the available approaches, the Analogue Method (AM) provides a practical reconstruction framework that has been successfully applied in the reconstruction of gridded climate fields (Bothe and Zorita, 2021; Pfister et al., 2020; Yiou et al., 2014; Franke et al., 2011). The core principle of AM is to search a pre-defined pool of model simulations for the field whose spatial anomaly pattern most closely matches the proxy-based anomaly pattern, and to use that field as the reconstruction. As a result, AM retains the dynamical consistency of climate model simulations while avoiding the computational burden associated with complex assimilation cycles.

In our previous study, we improved the AM for historical temperature reconstructions introducing methodological refinements (Zhang et al., 2025b). Specifically, we enhanced the analogue search process by incorporating two proxy-related terms, which improved the accuracy of analogue matching. Control experiments for EA over 1901-2000 demonstrated that the improved framework can reproduce historical temperature variations. Based on this validated approach, the present study develops a gridded temperature dataset for EA covering 1400-2000.

2 Data

As shown in Fig. 1, East Asia (EA) is located on the eastern margin of the Eurasian continent and adjacent to the Pacific Ocean. In this study, the study region covers 15°~55 ° N, 70°~150°E, mainly comprising China, Mongolia, the Korean Peninsula, and Japan. Topographically, EA is characterized by a distinct three-step pattern, with elevation decreasing from west to east. The region can be broadly divided into the western highlands and the eastern lowlands. The highest elevations, exceeding 4000 m, occur in the southwest and are associated with the Tibetan Plateau and the Himalayas, while the lowest elevations are found in the eastern coastal plains and basins.

https://doi.org/10.5194/essd-2026-295
Preprint. Discussion started: 23 June 2026

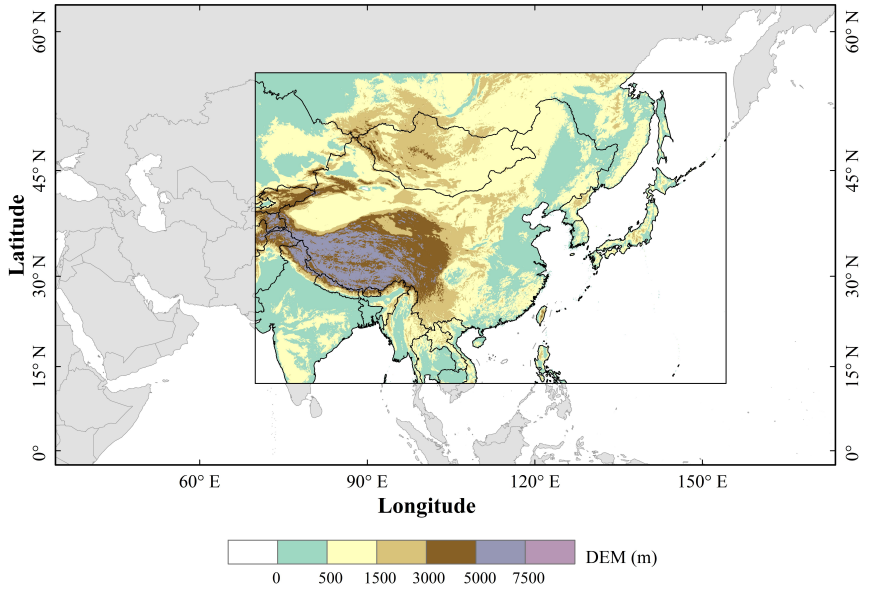

Figure 1: Map of the study area, East Asia (EA). Color shading indicates digital elevation model (DEM) values (units: m).

2.1 The proxy records

A total of 423 climate proxy records were collected from publicly available papers and monographs, ensuring that the data sources were transparent and traceable. Quality control criteria for the proxy records were as follows:

(1) Temporal coverage and resolution: Each proxy record must span at least 100 years, with a starting year no later than 1877 and an ending year no earlier than 1977. Only records with an annual temporal resolution were accepted.

(2) Geographical coverage: The proxy record must be located within the study area (70°~150°E, 15°~55°N).

(3) Type and prioritization: Tree-ring records were prioritized due to their clear annual resolution and high sensitivity to temperature variations.

(4) Correlation screening: Each proxy record was tested for correlation with the local annual mean temperature at the corresponding grid cell in the CRU dataset, with the annual mean defined from the previous October to the current September. Only records with statistically significant correlations ($p<0.05$) were retained.

After filtering, 119 high-quality proxy records were retained, including 108 tree-ring records, 7 temperature reconstructions from previous studies, 3 glacier ice records, and 1 historical document record (Table S1). These proxies provide spatial coverage across the study area (Fig. 2) and and substantial temporal coverage, with 19 records spanning the entire 1400-2000 period and all 119 records covering more than 100 years.

https://doi.org/10.5194/essd-2026-295
Preprint. Discussion started: 23 June 2026

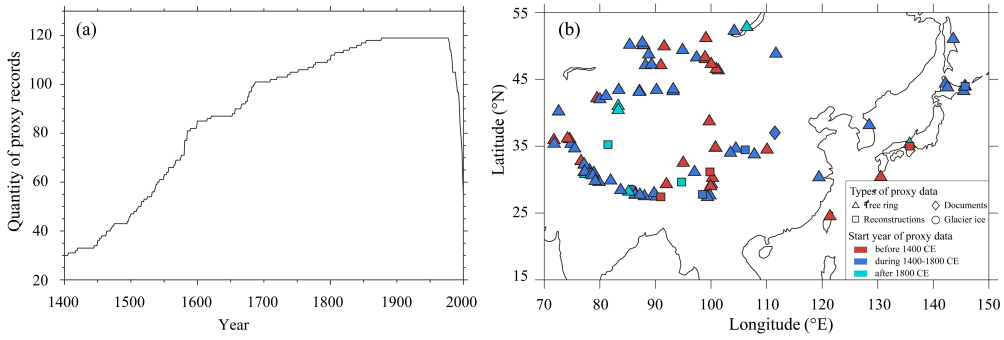

Figure 2: Characteristics of proxy records used for reconstruction. (a) Temporal variation in the number of available proxy records; (b) Types and spatial distribution of proxy records.

2.2 The simulated temperature data

The Coupled Model Intercomparison Project Phase 6 (CMIP6) is an initiative of the World Climate Research Programme (WCRP) that provides a standardized framework for evaluating Earth System Model (Eyring et al., 2016). By comparing simulations from multiple coupled climate models, CMIP6 facilitates a deeper understanding of the drivers and future trajectories of climate change. For historical climate studies, CMIP6 provides extensive spatial patterns of simulated temperature anomalies, which can be used to construct the analogue pool.

The Earth System Model outputs used in this study were selected according to a unified set of metadata criteria, including experiment IDs (historical and past1000), variant label (r1i1p1f1), grid label (gn), table ID (Amon), frequency (mon), and variable ID (tas). Based on these criteria, 37 models were selected from historical experiment, and 2 of them also participated in the PMIP4 past1000 experiment. The CMIP6 historical experiment spans 1850-2014, while the PMIP4 past1000 experiment covers 850-1850. Detailed information on the selected models is given in Appendix A.

2.3 The instrumental observations

The validation of reconstruction relied on the Climatic Research Unit (CRU) Time-Series (TS) version 4.04 dataset (Harris et al., 2020). This dataset offers spatially continuous global land climate fields derived from quality-controlled station observations. With a spatial resolution of 0.5°× 0.5° and monthly temporal resolution spanning 1901-2019, CRU TS 4.04 captures detailed regional climate variability, making it particularly suitable for assessing temperature variations over the complex terrain of EA. In this study, the monthly data were calculated to annual means (previous October to current September) to match the temporal resolution of the proxy network.

https://doi.org/10.5194/essd-2026-295
Preprint. Discussion started: 23 June 2026

3 Methodology

3.1 Analogue Method

The AM is based on the principle that similar predictor patterns (P) at different times are associated with similar predictand states (T). Therefore, historical observations of $T(t)$ can be used to estimate the unknown $T(t_0)$ when their predictor patterns $P(t)$ and $P(t_0)$ are statistically similar (Zorita and von Storch, 1999; Lorenz, 1969).

Specifically, the method requires the construction of an analogue pool based on historical paired observations $\{P(t_i), T(t_i)\}$. For a target period t_0 where only the predictor $P(t_0)$ is available, the similarity between $P(t_0)$ and each $P(t_i)$ in the pool is quantified, and the closest analogues are selected to estimate the unknown $T(t_0)$. The similarity metric is defined as:

$$\Delta(t_i)=dist(P(t_0), P(t_i)), \quad \forall i \in pool, \tag{1}$$

where $P(t_0)$ denotes the predictor state at target time t_0, and $P(t_i)$ represents the *i-th* predictor $P(t)$ in the analogue pool.

Several approaches have been proposed to quantify similarity in practical applications (Gómez-Navarro et al., 2017; Yun et al., 2021). In this study, we adopt an *RMSE*-based search strategy as this metric has been shown to perform robustly in capturing both spatial patterns and amplitude differences within complex climate fields. In practical climate reconstructions based on proxy records, the standard AM faces several challenges. These limitations mainly arise from the uneven spatial distribution of proxy records, the substantial temporal changes in proxy availability, and the differing sensitivities and biases among proxy types (Anchukaitis and Smerdon, 2022; Christiansen and Ljungqvist, 2017). To address these limitations and improve reconstruction accuracy, we introduce targeted modifications to the *RMSE*-based AM. Specifically, we develop an enhanced framework that integrates a correlation constraint (*CC*) and a modified RMSE optimization (*mRMSE*).

Correlation constraint. For each temperature field in the analogue pool, the pearson correlation coefficient (CC) was calculated between the simulated field t_m and the corresponding proxy-based observations t_p over the common grid points. Only analogues exhibiting a statistically significant positive spatial correlation ($CC>0$, $p<0.05$) were retained for further evaluation. Statistical significance was assessed using a two-sided Student's t-test. The formulas for *CC* is given below:

$$CC(t_p, t_m)=\frac{\sum_i^N (t_{p,i}-\overline{t_p})(t_{m,i}-\overline{t_m})}{\sqrt{\sum_i^N (t_{p,i}-\overline{t_p})^2}\sqrt{\sum_i^N (t_{m,i}-\overline{t_m})^2}} \tag{2}$$

where N denotes the number of grid points with available proxy records for a given year Y. $t_{p,i}$ and $t_{m,i}$ represent proxy values and simulated values at the i-th grid cell, respectively. The overbar denotes the spatial mean calculated over available N grid cells.

Then, two weighting terms were introduced to enhance the robustness of the *RMSE*-based search process: a variance-explained weight (v_p) and a spatial-density weight (k_p). The term v_p quantifies the ability of each proxy record to capture the variability of the target temperature series. It is defined as the fraction of instrumental temperature variance explained by the proxy during the calibration period, thereby assigning greater weight to records with higher temperature sensitivity. The term

https://doi.org/10.5194/essd-2026-295
Preprint. Discussion started: 23 June 2026

k_p is introduced to mitigate the influence of non-uniform spatial distribution among proxy sites. For each location, the sampling density is estimated using a Gaussian kernel density estimator. The resulting density field is then applied to downweight records in high-density clusters and upweight those in sparse regions, effectively reducing spatial sampling bias in the similarity calculation. By integrating these weighting terms, the modified objective search strategy (*mRMSE*) provides a weighted similarity measure optimized for selecting analogue candidates that accurately reflect the spatial patterns of historical temperature anomalies. The *mRMSE* is defined as follows:

$$mRMSE(t_p, t_m)=\sqrt{\frac{1}{n}\sum_{i=1}^{n} w_i\,(t_{p,i}-t_{m,i})^2} \tag{3}$$

$$w_i=\frac{v_p}{k_{p,i}} \tag{4}$$

where n is the number of available proxy records for a specific year; v_p is the variance-explained weight, defined as the squared correlation coefficient ($r_p{}^2$) between the proxy record and the CRU temperature during the calibration period; k_p is the spatial-density weight derived from a Gaussian kernel density estimator:

$$k_p=\frac{1}{n}\sum\frac{1}{2\pi h}e^{-\frac{d(g_i,g_j)^2}{2h^2}} \tag{5}$$

$$d(g_i, g_j)=2R\cdot\ acr\,sin\left(\sqrt{sin^2(\frac{\theta_j-\theta_i}{2})+\cos(\theta_i)\cos(\theta_j)sin^2(\frac{\lambda_j-\lambda_i}{2})}\right) \tag{6}$$

where h denotes the smoothing bandwidth (set to 300 km in this study) and $d(g_i, g_j)$ is the Great Circle distance between site i and j; R is the radius of the Earth, θ and λ are the radians corresponding to latitude and longitude, respectively.

3.2 Reconstruction process

The procedure for reconstructing the gridded temperature dataset is illustrated in Fig. 2 and involves two main steps: data preparation and gridded temperature reconstruction.

(1) Data preparation. The input data included temperature-sensitive proxy records, instrumental temperature fields, and simulated temperature fields. All datasets were harmonized over the EA domain (15°N~55°N, 70°E~150°E) through the following steps:

(i) Temporal and spatial harmonization. Monthly temperature data from modern instrumental records (CRU TS v4.04) and climate model simulations (CMIP6 historical/ PIMP4 past1000) were aggregated into annual means. It should be noted that most of the proxy records used in this study are tree-ring data, which primarily reflect temperature conditions during the biological growth year rather than the calendar year (Fang et al., 2022). Therefore, annual mean temperature was defined as the average from October of the previous year to September of the current year. The gridded instrumental and simulated temperature fields were then interpolated to a standard 1°×1° grid using a bilinear method.

(ii) Data standardization. For each proxy record and each grid-cell temperature series, standardization was performed using the z-score method (Eq. (7)). To ensure comparability among proxy records, instrumental data, and simulated data during

https://doi.org/10.5194/essd-2026-295
Preprint. Discussion started: 23 June 2026

analogue matching, all series were standardized over the common reference period of 1902-1977 using dataset-specific means and standard deviations. This period was selected as, under the growth-year definition adopted in this study (October of the previous year to September of the current year), 1902 is the first year for which a complete annual value can be derived from the CRU data, while 1977 is the last year covered by all proxy records used in the reconstruction. For the simulated data, PMIP4 and CMIP6 outputs from corresponding models were first concatenated and then standardized over the same reference period.

$$Z=\frac{X-\mu}{\sigma} \quad (7)$$

where X is the original data series, μ is the mean value of the series, σ is the standard deviation, and Z is the standardized series.

(2) Analogue pool construction. An analogue pool was constructed from simulated temperature fields derived from 37 Earth system models (ESMs) from the CMIP6/PMIP4 archives, yielding a total of 8,070 model years. Each simulated annual temperature field was treated as a candidate analogue. After temporal and spatial harmonization, all model-derived temperature fields were assembled into an analogue pool that representing a wide range of temperature anomaly patterns over EA.

(3) Gridded temperature reconstruction. The gridded temperature field for EA was reconstructed year by year using the improved Analogue Method (AM), following the steps below.

(i) Construction of the target-year proxy vector. For each target year, all available proxy records were extracted and assembled into a proxy vector. The number of proxy records used in the reconstruction therefore varied among years depending on data availability.

(ii) Calculation of proxy weights. For each proxy record, the weighting terms required by the improved AM were first determined. The spatial-density weight k_p was calculated using Eq. (5). The variance-explained weight (v_p) was calculated from the overlapping period between each proxy series and the corresponding CRU temperature series at the same grid cell. These two terms were then combined to obtain the proxy weight w according to Eq. (4).

(iii) Searching in the analogue pool. For each target year, the proxy vector was compared with all candidate analogue years in the analogue pool. For each candidate analogue, the simulated temperature values at the grid cells corresponding to the proxy locations were extracted to form an analogue vector. The correlation coefficient (*CC*) between the proxy vector and each candidate analogue vector was first calculated using Eq. (2). Only candidates with positive correlation ($CC>0$) were retained for further comparison.

(iv) Selection of the optimal analogue. For the retained candidate analogues, the *mRMSE* was calculated using Eq. (3), and then ranked according to their *mRMSE* values. The optimal analogue for the target year was selected as the candidate with the minimum *mRMSE*.

https://doi.org/10.5194/essd-2026-295
Preprint. Discussion started: 23 June 2026

Open Access Earth System Science Data Discussions

(v) Reconstruction of the gridded temperature field. The full gridded temperature field corresponding to the optimal analogue was then taken as the reconstructed standardized temperature field for that year. This procedure was repeated for all target years to produce a continuous standardized gridded temperature reconstruction for EA during 1400-2000.

(vi) Conversion of standardized reconstructions to physical temperature units. As analogue matching and reconstruction were performed in standardized space, the reconstructed fields were finally transformed back to physical temperature units. Specifically, the standardized reconstructed fields were multiplied by the grid-cell standard deviation and then added to the corresponding grid-cell mean derived from the CRU dataset over the reference period 1902-1977.

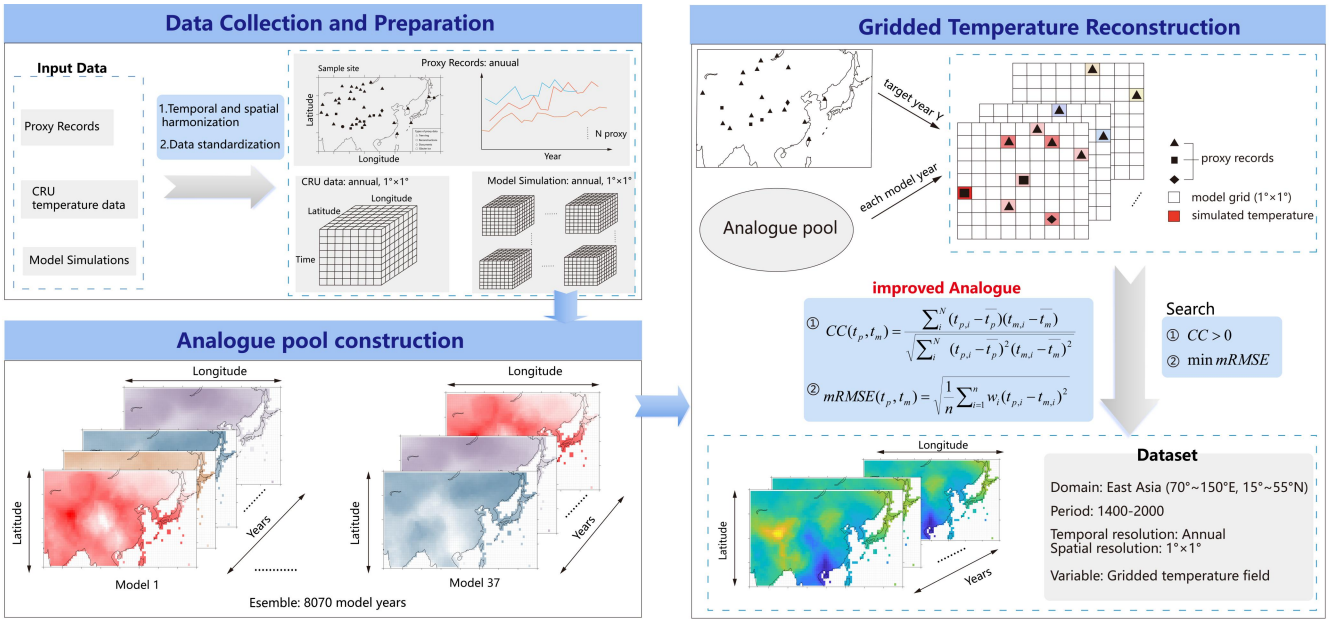

Figure 3: Flowchart of the gridded temperature reconstruction.

3.3 Statistical analysis

Statistical analysis including piecewise linear fitting (Muggeo, 2003), moving-average smoothing, linear trends, significance testing (Santer et al., 2000), empirical orthogonal function (EOF) analysis (Lorenz, 1956), and the North test (North et al., 1982) were applied to characterize the temporal variation and spatial patterns of temperature. Piecewise linear fitting was used to identify possible transition points in the regional mean temperature series and to quantify trend differences among successive periods. Moving-average smoothing was used to reduce short-term fluctuations and highlight low-frequency variability, with each smoothed value assigned to the midpoint year of the corresponding moving window. Linear trends were calculated for the full period and selected subperiods to quantify the direction and magnitude of temperature variation. Statistical significance was evaluated for the main results, including trends, correlations, and regressions, with a significance level of 0.05 unless otherwise stated. EOF analysis was performed on the gridded temperature anomaly field to extract the

https://doi.org/10.5194/essd-2026-295
Preprint. Discussion started: 23 June 2026

leading modes of spatial variability and their corresponding principal component (PC) time series, and the North test was further applied to assess whether adjacent eigenvalues were significantly separated.

4 Results

4.1 Validation of the reconstructed temperature field

4.1.1 Comparison of temporal variations and dominant spatial modes

Over the overlapping period (1901-2000), the reconstructed temperature series agrees well with the CRU temperature series in terms of long-term variation (Fig. 3). Both series exhibit a significant warming trend, with liner trend of 2.95 °C/100 a and 2.23°C/100 a for the reconstruction and CRU, respectively. The two series are significantly correlated ($r=0.74$, $p<0.01$), indicating that the reconstruction captures the main temporal variation of observed temperature changes.

A two-breakpoint segmented regression applied to the 9-year smoothed CRU series identified breakpoints in 1947 and 1973, dividing the 20th-century variation into three broad phases: an early warming phase (1901-1947), a mid-century fluctuated cooling phase (1948-1973), and a late-century rapid warming phase (1974-2000). During 1901-1947, both the reconstructed and CRU series show a warming trend, although the warming rate is weaker in the reconstruction (0.04 °C/10 a) than in CRU (0.08 °C/10 a). During 1948-1973, both series exhibit fluctuated cooling, with trends of -0.04 °C/10 a for the reconstruction and -0.01 °C/10 a for CRU. During 1974-2000, both series show rapid warming, but the warming rate in the reconstruction (0.17 °C/10 a) remains lower than that in CRU (0.30 °C/10 a).

The reconstructed series also shows a smaller range than CRU in all three phases, with values of 0.83, 0.64, and 0.64 °C, compared with 0.89, 0.91, and 1.43 °C for CRU during 1901-1947, 1948-1973, and 1974-2000, respectively. This indicates that the reconstruction captures the major phase transitions of 20th-century temperature variation, but underestimates the magnitude of observed variability.

https://doi.org/10.5194/essd-2026-295
Preprint. Discussion started: 23 June 2026

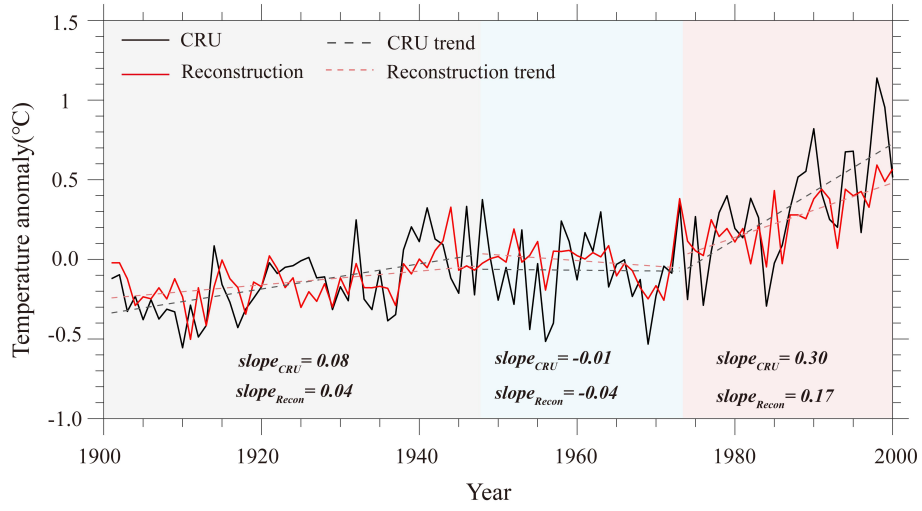

Figure 4: Temporal variations (units: ℃) and piecewise linear trends(units: ℃/10 a) of the reconstructed and CRU temperature anomaly series. Gray, blue, and red shading denote the three phases identified from segmented regression.

The EOF analysis indicates that the reconstruction reproduces the leading mode of temperature variability well, whereas its agreement with the CRU data becomes weaker for the higher-order modes. Specifically, the first EOF mode (EOF1) of the reconstructed temperature field over EA during 1901-2000 is highly consistent with that of the CRU data. EOF1 accounts for 33.6% and 40.7% of the total variance for the reconstruction and CRU data, respectively. Both datasets exhibit a spatially coherent monopole pattern across the region (Fig. 5a, 5d), with the largest loadings located north of 35°N, indicating that northern China and Inner Mongolia contribute most strongly to the leading warming mode. The corresponding PC1 time series of the reconstruction and CRU data are highly correlated ($r=0.75$, $p<0.05$) and show an increasingly trend, consistent with the 20th-century warming (Fig. 5g).

The second mode (EOF2) explains 18.6% of the variance in the reconstructed temperature, compared with 10.3% in the CRU data. In both datasets, EOF2 is characterized by a north-south dipole pattern (Fig. 5b, 5e). The positive centers are similarly located over Northeast China, whereas the negative centers differ in position. In the CRU data, the negative center is located over inland China, specifically Qinghai and Gansu (Fig. 5b), while in the reconstruction it shifts southward to southern China (Fig. 5e). The corresponding PC2 time series of the reconstruction and CRU data are positively correlated (Fig. 5h), yet weakly ($r=0.22$, $p<0.05$), suggesting that the reconstruction captures the main dipole structure of EOF2 but with notable spatial biases.

The third mode (EOF3) accounts for 8.4% and 6.5% of the variance in the reconstructed temperature and CRU data, respectively, and both exhibit a tripolar spatial structure (Fig. 5c, 5f). In the CRU data, negative centers are located over Northeast China and the Tibetan Plateau, while the positive center is situated over northwestern EA. In contrast, the reconstructed EOF3 shows negative centers over Northeast China and southwestern EA, and its positive center a southeast-northwest-oriented band extending from southern to northwestern China. The corresponding PC3 time series of the

https://doi.org/10.5194/essd-2026-295
Preprint. Discussion started: 23 June 2026

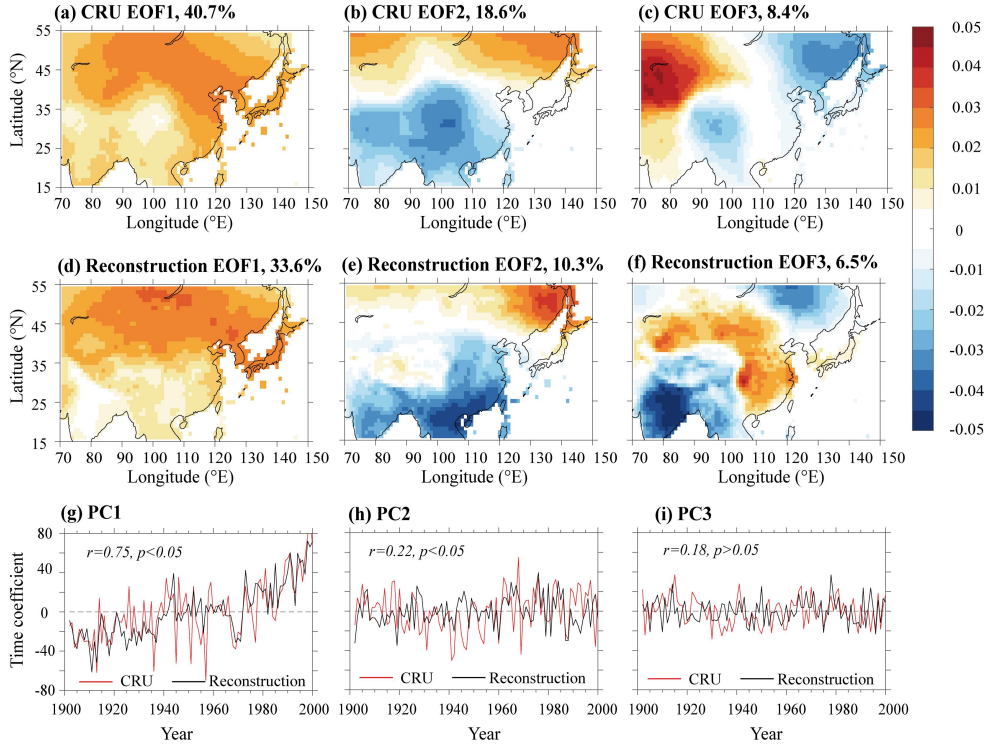

Figure 5: First three EOF modes (1901-2000). (a-c) CRU, (d-f) Reconstruction (g-i) Corresponding temporal coefficients (PCs) for reconstructed and CRU data.

reconstruction and CRU data both show modest decadal variability (Fig. 5i), but their correlation is weak and not statistically significant ($r=0.18$, $p>0.05$), indicating limited agreement between the two datasets for this higher-order mode.

4.1.2 Correlation-based validation of temporal variations and spatial patterns

To further assess reconstruction skill, we calculated (1) year-by-year spatial correlations between the reconstructed and CRU temperature fields, and (2) grid-point temporal correlations between the two datasets over the overlapping period (1901-2000).

The year-by-year spatial correlations indicate that the reconstructed and CRU temperature fields generally exhibit similar spatial patterns during the 1901-2000 overlapping period (Fig. 6a). Significant positive correlations ($p<0.05$) are found in 72% of the years, with a maximum correlation coefficient of 0.74. By contrast, significant negative correlations ($p<0.05$) occur in only 24% of the years, with a minimum coefficient of -0.49, while the remaining years show no significant correlation.

The spatial distribution of the grid-point correlation coefficients (Fig. 6b) further supports the overall skill of the reconstruction. Of the 2338 valid grid cells, 82.7% show a significant positive correlation ($p<0.05$). The higher correlations ($r>0.6$, $p<0.05$) are concentrated in Japan, Northeast China, the Tibetan Plateau, and Mongolia, many of which coincide with regions of relatively dense proxy coverage (Fig. 6b).

https://doi.org/10.5194/essd-2026-295
Preprint. Discussion started: 23 June 2026

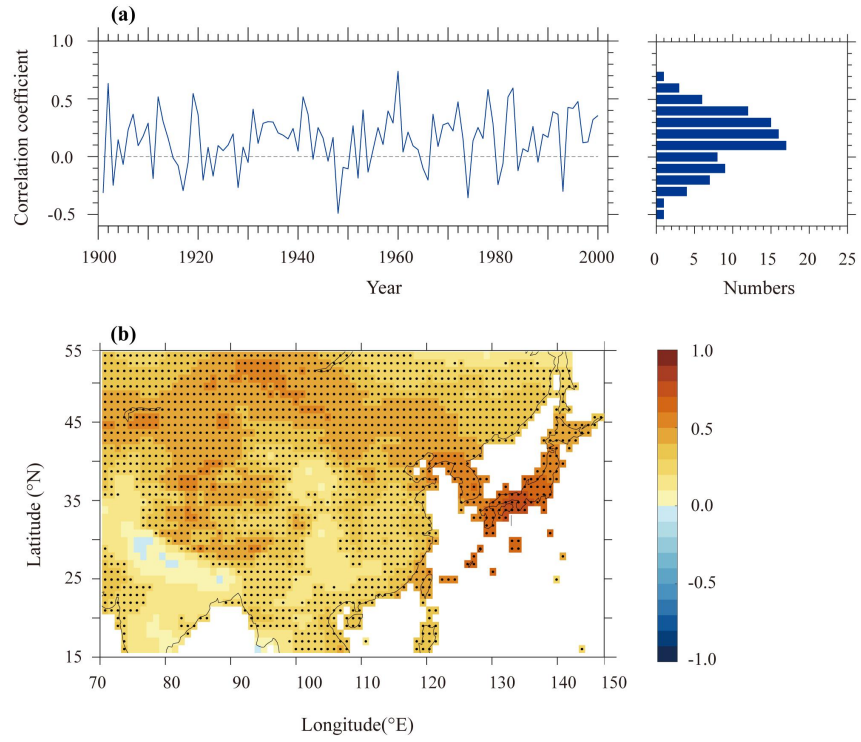

Figure 6: Spatial distribution of correlation coefficients between Reconstruction and CRU data. Black dots indicate statistically significant correlations (p<0.05).

4.2 The temporal variations of temperature in EA over the past 600 years

The reconstructed gridded dataset was used to examine regional temperature variations in EA during 1400-2000.. Regional temperature variation can be divided into three broad phases: a cooling phase, a period of fluctuation, and a warming phase (Fig. 7a). The initial cooling period (1400-1510) was characterized by a significant decreasing trend at a rate of -0.27 °C/100 a. This was followed by a period of fluctuation (1511-1844), during which the temperature trend was minimal and not statistically significant (0.02 °C/100 a). The final period (1845-2000) marked a shift to a rapid warming trend, with temperatures increasing at a rate of 0.34 °C/100 a.

To further characterize centennial-scale variability, a 101-year sliding trend analysis was performed (Fig. 7b), which identifies six alternating cooling and warming episodes. Three cooling episodes were identified (1450-1515, 1639-1679, and 1763-1835), with peak cooling rates of -0.31 °C/100 a, -0.18 °C/100 a, and -0.25 °C/100 a, respectively. These cooling episodes were separated by three warming episodes. The first two warming episodes (1516-1638 and 1680-1762) reached peak warming rates of 0.17 °C/100 a and 0.21 °C/100 a, respectively. The third warming episode (1836-1950) was substantially stronger than the preceding warming episodes. It was characterized by sustained warming, with the sliding trend reaching approximately 0.58 °C/100 a around 1950, the highest rate observed during the past 600 years.

https://doi.org/10.5194/essd-2026-295
Preprint. Discussion started: 23 June 2026

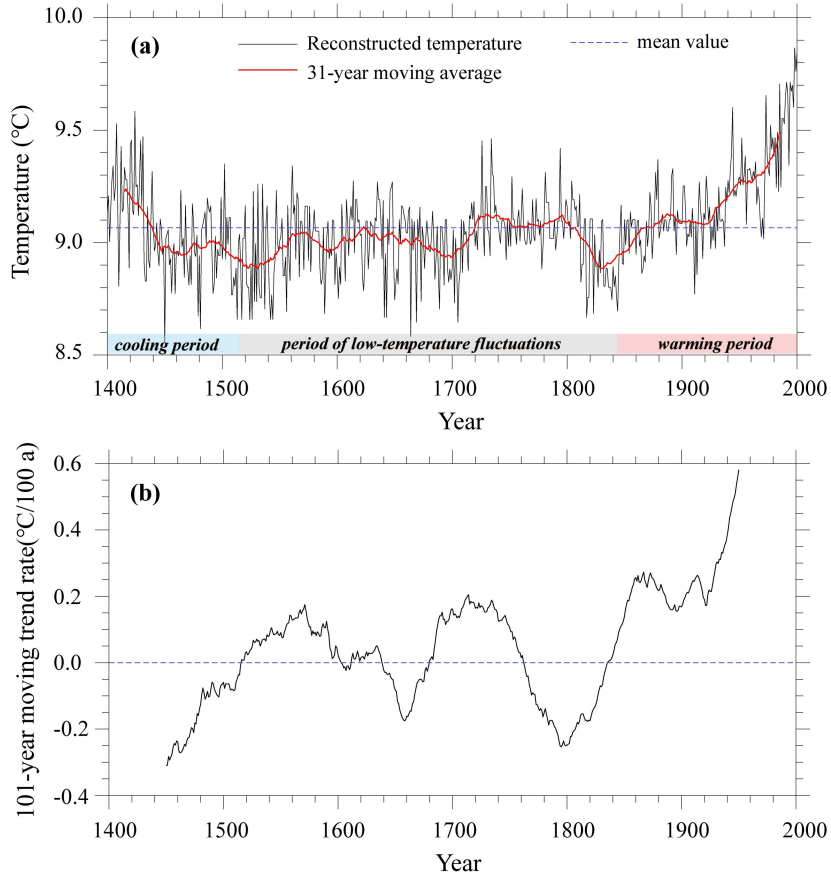

Figure 7: Annual mean temperature over EA (1400-2000). (a) Temporal variation; (b) Temporal variation with a 101-year moving trend.

4.3 The spatial patterns of temperature in EA over the past 600 years

To characterize the dominant modes of spatial variability in the reconstructed temperature field, we applied EOF analysis. According to the North test, the first three EOF modes are statistically separable (Table S2). They explain 52.7% of the total variance and therefore capture the major features of temperature variability over EA during the past 600 years. The spatial patterns of these three leading modes and their corresponding principal components (PCs) are shown in Fig. 8.

The first mode (EOF1) explains 26.3% of the total variance and exhibits a monopole-like pattern, with positive loadings across the entire study area (Fig. 8a). The largest loadings occur north of 40°N, particularly over the Mongolian Plateau and

https://doi.org/10.5194/essd-2026-295
Preprint. Discussion started: 23 June 2026

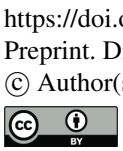

Open Access Earth System Science Data Discussions

Northeast China, indicating that temperature variations in these regions contribute strongly to this mode. The corresponding PC1 shows a marked long-term upward trend over the past 600 years(Fig. 8d) and closely resembles the EA mean temperature series shown in Fig. 7. This result indicates that EOF1 represents the dominant mode of large-scale temperature variability and primarily reflects the long-term warming signal across the study area.

The second mode (EOF2), accounting for 11.2% of the total variance, displays a dipole-like spatial structure (Fig. 8b). Positive loadings are centered over Northeast China, whereas negative loadings are concentrated over southern China, especially Guangdong and Hainan. By contrast, the loadings over the Tibetan Plateau are relatively weak. The corresponding PC2 is characterized by evident temporal fluctuations but shows no clear long-term trend (Fig. 8e). This suggests that EOF2 mainly reflects regional temperature contrasts rather than a persistent large-scale warming pattern.

The third mode (EOF3) explains 7.5% of the total variance and also shows a dipole-like pattern (Fig. 8c). Positive loadings are located in the northwestern part of the study area, whereas negative loadings extend from the southeastern coast of China to South China. Compared with PC1 and PC2, PC3 has a smaller amplitude and weaker temporal variability (Fig. 8f), indicating that EOF3 represents a higher-order and relatively weak mode of regional temperature heterogeneity.

Overall, the EOF results show that temperature variation in EA over the past 600 years is dominated by a coherent large-scale warming mode, while the second and third modes mainly describe regional contrast patterns superimposed on the long-term background change.

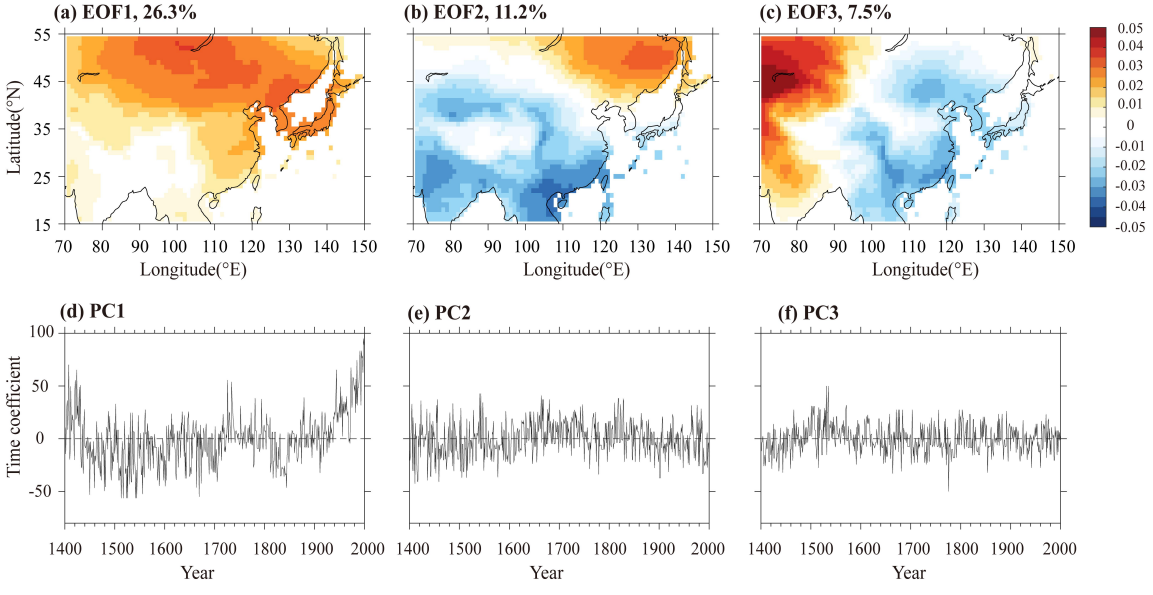

Figure 8: Spatial patterns and temporal coefficients of the first three EOF modes for reconstructed EA temperature (1400-2000).

https://doi.org/10.5194/essd-2026-295
Preprint. Discussion started: 23 June 2026

5 Discussion

Our reconstruction indicates that EA temperature variability was closely linked to large-scale climate change over the past 600 years. The EA series is significantly correlated with the global (Neukom et al., 2019) and Northern Hemisphere (Fang et al., 2022) reconstructions, with correlation coefficients of 0.65 and 0.50, respectively ($p<0.05$; Fig. 9a,b), indicating that it contains a strong common signal of temperature variation. The long-term warming trend in the EA reconstruction is 0.19 °C/100 a, which is comparable to those in the global and Northern Hemisphere reconstructions (0.25 and 0.14 °C/100 a, respectively). This consistency is physically reasonable, as large-scale external forcing can produce a shared low-frequency background across regions, while regional variability is superimposed on this background (Anchukaitis and Smerdon, 2022). However, coherence with large-scale reconstructions does not imply identical timing of extremes across regions. Our reconstruction indicates a temperature minimum in the mid-19th century, and this feature should not be regarded as inconsistent with Neukom et al. (2019). Their study emphasized that preindustrial warm and cold periods were not globally synchronous, and that the coldest interval occurred in different centuries in different regions; notably, the mid-nineteenth century was the most likely coldest interval for most regions outside the central and eastern Pacific, northwestern Europe, and southeastern North America. In this context, the EA minimum identified here is more appropriately interpreted as a regional expression of late preindustrial cooling. A plausible explanation is that the EA response was further modulated by regional climatic processes, especially monsoon variability and land-sea thermal contrast, both of which are important controls on temperature variation in this region(Neukom et al., 2019; Yang et al., 2020). Model-based studies also suggest that a weaker EA summer monsoon during the Little Ice Age was associated with reduced land-sea thermal contrast, lending support to a regionally modulated cooling signal. (Yang et al., 2020; Man et al., 2012).

Comparison with the Asian and China reconstructions suggests that the remaining similarities and discrepancies likely reflect both real regional climate structure and differences in reconstruction design. The Asian summer temperature reconstruction of Shi et al. (2015) highlighted substantial spatial and temporal variation across eastern and south-central Asia, while the China reconstruction of Ge et al. (2013) was developed from proxy records in five regions and therefore places stronger emphasis on regional heterogeneity. By contrast, the reconstructed EA mean series is better suited to extracting the common signal shared across the study domain, but it inevitably smooths subregional variability. For this reason, differences between our reconstruction and previous Asian or China-wide series should not be attributed solely to methodological artifacts, nor should they be interpreted solely as evidence of climatic divergence. More likely, they arise from the combined effects of regional climate heterogeneity, proxy type, spatial coverage, temporal resolution, and reconstruction method. This interpretation is also consistent with recent reviews showing that proxy distribution and methodological choices remain major sources of uncertainty in the recovery of low-frequency variability in large-scale paleotemperature reconstructions. (Shi et al., 2015; Ge et al., 2013; Anchukaitis and Smerdon, 2022).

https://doi.org/10.5194/essd-2026-295
Preprint. Discussion started: 23 June 2026

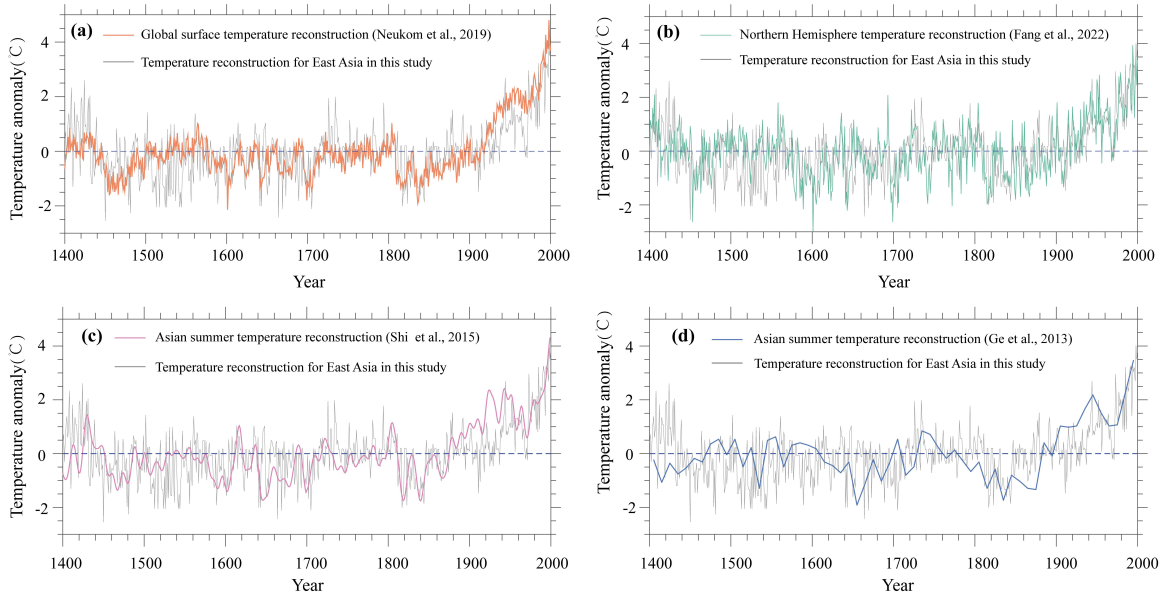

Figure 9: Comparison of EA temperature reconstruction with previous reconstructions (1400-2000). (a) Global surface temperature(Neukom et al., 2019); (b) Northern hemisphere temperature(Fang et al., 2022); (c) Asian summer temperature(Shi et al., 2015); (d) China temperature(Ge et al., 2013).

6 Conclusions

Temperature is one of the most direct indicators of long-term climate change. Therefore, developing robust gridded datasets for past centuries is essential multi-scale climate analysis the assessment of extreme climate risks. In this study, we reconstructed a gridded temperature dataset for East Asia (EA) from 1400 to 2000 at 1°×1° spatial and annual temporal resolution using an improved Analogue Method (AM) that integrates climate proxy records with climate model simulations. The reconstructed temperature field is consistent with instrumental observations during the overlapping period (1901-2000), with a temporal correlation coefficient of $r=0.74$ ($p<0.01$), supporting the reliability of the reconstruction. The reconstructed dataset reveals three distinct phases of temperature variation in EA over the past six centuries: a cooling phase (1400-1510), a fluctuating cold phase (1511-1844), and a warming phase (1845-2000). At the centennial scale, the strongest cooling and warming trends occurred during 1400-1500 (-0.31 °C/100 a) and 1900-2000 (0.58 °C/100 a), respectively. In spatial terms, the largest temperature variability was concentrated in the core region of the Siberian High.

This dataset provides an important basis for investigating the spatiotemporal characteristics and multi-scale variation of temperature in EA, thereby supporting further advances in regional paleoclimate research. Future work should focus on several key directions. Although this study identifies distinct centennial-scale phases, the relative roles of natural and anthropogenic forcings across different timescales remain to be assessed. In addition, expanding the proxy network, especially in data-sparse regions, and developing seasonal reconstructions will provide deeper insights into the spatiotemporal heterogeneity of climate variability in EA. Moreover, establishing objective criteria for selecting climate

https://doi.org/10.5194/essd-2026-295
Preprint. Discussion started: 23 June 2026

models that perform well in simulating the target region remains a methodological priority for improving the reconstruction of regional climatic patterns.

Appendix A

Table A1: List of Earth System Models used in this study

No.	Model Name	Institution	Time period & Experiment(s)
1	ACCESS-CM2	Commonwealth Scientific and Industrial Research Organisation, Australia	1850-2014 (CMIP6 Historical)
2	AWI-CM-1-1-MR	Alfred Wegener Institute, Helmholtz Centre for Polar and Marine Research, Germany	1850-2014 (CMIP6 Historical)
3	AWI-ESM-1-1-LR		1850-2014 (CMIP6 Historical)
4	BCC-CSM2-MR	Beijing Climate Center, China	1850-2014 (CMIP6 Historical)
5	BCC-ESM1		1850-2014 (CMIP6 Historical)
6	CAMS-CSM1-0	Chinese Academy of Meteorological Sciences, China	1850-2014 (CMIP6 Historical)
7	CanESM5	Canadian Centre for Climate Modelling and Analysis, Environment and Climate Change Canada, Canada	1850-2014 (CMIP6 Historical)
8	CanESM5-1		1850-2014 (CMIP6 Historical)
9	CAS-ESM2-0	Chinese Academy of Sciences, China	1850-2014 (CMIP6 Historical)
10	CESM2	National Center for Atmospheric Research, Climate and Global Dynamics Laboratory, USA	1850-2014 (CMIP6 Historical)
11	CESM2-FV2		1850-2014 (CMIP6 Historical)
12	CESM2-WACCM		1850-2014 (CMIP6 Historical)
13	CESM2-WACCM-FV2		1850-2014 (CMIP6 Historical)
14	CMCC-CM2-HR4	Fondazione Centro Euro-Mediterraneo sui Cambiamenti Climatici, Italy	1850-2014 (CMIP6 Historical)
15	CMCC-CM2-SR5		1850-2014 (CMIP6 Historical)
16	CMCC-ESM2		1850-2014 (CMIP6 Historical)
17	FGOALS-g3	Chinese Academy of Sciences, China	1850-2014 (CMIP6 Historical)
18	FIO-ESM-2-0	First Institute of Oceanography, Ministry of Natural Resources, China, and Qingdao National Laboratory for Marine Science and Technology, China	1850-2014 (CMIP6 Historical)
19	GISS-E2-1-G	Goddard Institute for Space Studies, USA	1850-2014 (CMIP6 Historical)
20	GISS-E2-1-G-CC		1850-2014 (CMIP6 Historical)
21	GISS-E2-1-H		1850-2014 (CMIP6 Historical)
22	GISS-E2-2-G		1850-2014 (CMIP6 Historical)
23	GISS-E2-2-H		1850-2014 (CMIP6 Historical)
24	IITM-ESM	Indian Institute of Tropical Meteorology, India	1850-2014 (CMIP6 Historical)
25	MCM-UA-1-0	Department of Geosciences, University of Arizona, USA	1850-2014 (CMIP6 Historical)
26	MIROC6	Japan Agency for Marine-Earth Science and Technology; Atmosphere and Ocean Research Institute, The University of Tokyo; National Institute for Environmental Studies; and RIKEN Center for Computational Science, Japan	1850-2014 (CMIP6 Historical)
27	MPI-ESM-1-2-HAM	HAMMOZ Consortium: ETH Zurich; Max Planck Institute for Meteorology; Forschungszentrum Jülich; University of Oxford; Finnish Meteorological Institute; Leibniz Institute for Tropospheric Research; and Center for Climate Systems Modeling (C2SM) at	1850-2014 (CMIP6 Historical)

https://doi.org/10.5194/essd-2026-295
Preprint. Discussion started: 23 June 2026

		ETH Zurich	
28	MPI-ESM1-2-HR	Max Planck Institute for Meteorology, Germany	1850-2014 (CMIP6 Historical)
29	MPI-ESM1-2-LR		1850-2014 (CMIP6 Historical)
30	NESM3	Nanjing University of Information Science and Technology, China	1850-2014 (CMIP6 Historical)
31	NorCPM1	NorESM Climate Modelling Consortium, Norway	1850-2014 (CMIP6 Historical)
32	NorESM2-LM		1850-2014 (CMIP6 Historical)
33	NorESM2-MM		1850-2014 (CMIP6 Historical)
34	SAM0-UNICON	Seoul National University, Republic of Korea	1850-2014 (CMIP6 Historical)
35	TaiESM1	Research Center for Environmental Changes, Academia Sinica, Taiwan	1850-2014 (CMIP6 Historical)
36	ACCESS-ESM1-5	Commonwealth Scientific and Industrial Research Organisation, Australia	850-2014 (CMIP6 Historical & PMIP4 past1000)
37	MRI-ESM2-0	Meteorological Research Institute, Japan	850-2014 (CMIP6 Historical & PMIP4 past1000)

Code and data availability

All data and code supporting this study are publicly available. The original gridded instrumental temperature data were obtained from the Climatic Research Unit (CRU) of the University of East Anglia, UK (https://www.uea.ac.uk/groups-and-centres/climatic-research-unit). The modelling temperature data were obtained from the Coupled Model Intercomparison Project Phase 6 (CMIP6) and can be accessed from https://aims2.llnl.gov/search/cmip6/. The historical multiproxy climate dataset was obtained from the PAGES 2k consortium (https://pastglobalchanges.org/). The processed input data used in this study, the reconstruction code, and the gridded temperature dataset generated in this study are openly available from Zenodo at https://doi.org/10.5281/zenodo.18477496 (Yan et al, 2026). The archived files are provided in .m/.mat format and distributed as .zip packages.

Supplement link

The link to the supplement will be included by Copernicus, if applicable.

Author contributions

XY: data curation, formal analysis, investigation, validation, visualization, software, writing-original draft, writing-review and editing. **XZ**: conceptualization, funding acquisition, project administration, supervision, software, writing-review and editing. **LZ**: funding acquisition, project administration, supervision.

https://doi.org/10.5194/essd-2026-295
Preprint. Discussion started: 23 June 2026

Open Access Earth System Science Data Discussions

Competing interests

The contact author has declared that none of the authors has any competing interests.

Disclaimer

Publisher's note: Copernicus Publications remains neutral with regard to jurisdictional claims made in the text, published maps, institutional affiliations, or any other geographical representation in this paper. While Copernicus Publications makes every effort to include appropriate place names, the final responsibility lies with the authors. Views expressed in the text are those of the authors and do not necessarily reflect the views of the publisher.

Acknowledgements

We acknowledge the Climatic Research Unit (CRU) at the University of East Anglia, the modelling groups participating in the Coupled Model Intercomparison Project Phase 6 (CMIP6) and PMIP4, the PAGES 2k consortium, and the providers of the Shuttle Radar Topography Mission (SRTM) digital elevation data for making the instrumental temperature data, climate model simulations, multiproxy datasets, and elevation data used in this study publicly available. We also thank Neukom et al. (2019), Fang et al. (2022), Shi et al. (2015) and Ge et al. (2013) for making their temperature reconstruction products at global and regional scales publicly available. These openly accessible datasets provided the essential basis for the reconstruction, evaluation, and comparison analysis conducted in this study.

Financial support

This research has been supported by the National Key R&D Program of China (grant: No.2022YFF0801103), and National Natural Science Foundation of China (grant: 42275043).

Review statement

The review statement will be added by Copernicus Publications listing the handling editor as well as all contributing referees according to their status anonymous or identified.

https://doi.org/10.5194/essd-2026-295
Preprint. Discussion started: 23 June 2026

References

Anchukaitis, K. J., and Smerdon J. E.: Progress and uncertainties in global and hemispheric temperature reconstructions of the Common Era, Quaternary Science Reviews, 286, 15, 107537. https://doi.org/10.1016/j.quascirev.2022.107537, 2022.

Anderson, D. M., Tardif, R., Horlick, K., P. Erb, M., Hakim, G. J., and Noone, D.: Additions to the Last Millennium Reanalysis multi-proxy database, Data Journal Science, 18, 2, https://doi.org/10.5334/dsj-2019-002, 2019.

Berner, J., Achatz, U., Batté, L., Bengtsson, L., Cámara, A. d. l., Christensen, H. M., Colangeli, M., Coleman, D. R. B., Crommelin, D., Dolaptchiev, S. I., Franzke, C. L. E., Friederichs, P., Imkeller, P., Järvinen, H., Juricke, S., Kitsios, V., Lott, F., Lucarini, V., Mahajan, S., Palmer, T. N., Penland, C., Sakradzija, M., von Storch, J., Weisheimer, A., Weniger, M., Williams, P. D., and Yano, J.: Stochastic Parameterization: Toward a New View of Weather and Climate Models, Bulletin of the American Meteorological Society, 98, 3, 565-588. https://doi.org/10.1175/BAMS-D-15-00268.1, 2017.

Bhend, J., Franke, J., Folini, D., Wild, M., and Brönnimann, S.: An ensemble-based approach to climate reconstructions, Climate of the Past, 8, 3, 963-976, https://doi.org/10.5194/cp-8-963-2012, 2012.

Bothe, O., and Zorita, E.: Technical note: Considerations on using uncertain proxies in the analogue method for spatiotemporal reconstructions of millennial-scale climate, Climate of the Past, 17, 2, 721-751, https://doi.org/10.5194/cp-17-721-2021, 2021.

Cao, F., Dan, L., Ma, Z. G., and Gao T.: The impact of land use and land cover change on regional climate over East Asia during 1980-2010 using a coupled model, Theoretical And Applied Climatology, 145, 549-565, https://doi.org/10.1007/s00704-021-03629-6, 2021.

Cao, L., Zhao, P., Yan, Z., Jones, P., Zhu, Y., Yu, Y., and Tang G.: Instrumental temperature series in eastern and central China back to the nineteenth century, J. Geophys. Res. Atmos., 118, 8197-8207, https://doi.org/10.1002/jgrd.50615, 2013.

Chen, X., Xing P., Luo, Y., Nie, S., Zhao, Z., Huang, J., and Tian, Q.: Multiscale combination of climate model simulations and proxy records over the last millennium, Theoretical and Applied Climatology, 132, 3-4, 763-777, https://doi.org/10.1007/s00704-017-2119-4, 2018.

Christiansen, B., and Ljungqvist, F. C.: Challenges and perspectives for large-scale temperature reconstructions of the past two millennia, Rev. Geophys., 55, 40-96, https://doi.org/10.1002/2016RG000521, 2017.

Cook, E. R., D'Arrigo, R. D., and Mann, M. E.: A well-verified, multiproxy reconstruction of the winter North Atlantic Oscillation index since AD 1400, Journal of Climate, 15, 1754-1764, https://doi.org/10.1175/1520-0442(2002)015<1754:AWVMRO>2.0.CO;2, 2002.

Cook, E. R., Krusic, P. J., Anchukaitis, K. J., Buckley, B. M., Nakatsuka, T., and Sano, M.: Tree-ring reconstructed summer temperature anomalies for temperate East Asia since 800 CE, Climate Dynamics, 41,11-12, 2957-2972, https://doi.org/10.1007/s00382-012-1611-x, 2013.

https://doi.org/10.5194/essd-2026-295
Preprint. Discussion started: 23 June 2026

Cook, E. R., Woodhouse, C. A., Eakin, C. M., Meko, D. M., and Stahle D. W.: Long-Term Aridity Changes in the Western United States, Science, 306, 5698, 1015-1018, https://www.science.org/doi/10.1126/science.1102586, 2004.

Deser, C., Lehner, F., Rodgers, K. B., Ault, T., Delworth, T. L., DiNezio, P. N., Fiore, A., Frankignoul, C., Fyfe, J. C., Horton, D. E., Kay, J. E., Knutti, R., Lovenduski, N. S., Marotzke, J., McKinnon, K. A., Minobe, S., Randerson, J., Screen, J. A., Simpson, I. R., Ting, M., and Capotondi, A.: Insights from Earth system model initial-condition large ensembles and future prospects, Nature Climate Change, 10, 4, 277-286, https://doi.org/10.1038/s41558-020-0854-5, 2020.

Eyring, V., Bony, S., Meehl, G. A., Senior, C. A., Stevens, B., Stouffer, R. J., and Taylor, K. E.: Overview of the Coupled Model Intercomparison Project Phase 6 (CMIP6) experimental design and organization, Geosci. Model Dev., 9, 1937-1958, https://doi.org/10.5194/gmd-9-1937-2016, 2016.

Fang, M., Li, X., Chen, H. W., and Chen, D. L.: Arctic amplification modulated by Atlantic Multidecadal Oscillation and greenhouse forcing on multidecadal to century scales, Nature Communications, 13, 1865, https://doi.org/10.1038/s41467-022-29523-x, 2022.

Franke, J, González-Rouco, J. F., Frank, D., and Graham N. E.: 200 years of European temperature variability: insights from and tests of the proxy surrogate reconstruction analog method, Climate Dynamics, 37, 133-150, https://doi.org/10.1007/s00382-010-0802-6, 2011.

Freund, M. B., Helle, G., Balting, D. F., Ballis, N., Schleser G. H., and Cubasch U.: European tree-ring isotopes indicate unusual recent hydroclimate, Commun. Earth Environ., 4, 26, https://doi.org/10.1038/s43247-022-00648-7, 2023.

Ge, Q., Hao, Z., Zheng, J., and Shao X.: Temperature changes over the past 2000 yr in China and comparison with the Northern Hemisphere, Climate of the Past, 9, 3, 1153-1160, https://doi.org/10.5194/cp-9-1153-2013, 2013.

Gómez-Navarro, J. J., Zorita, E., Raible, C. C., and Neukom, R.: Pseudo-proxy tests of the analogue method to reconstruct spatially resolved global temperature during the Common Era, Climate of the Past, 13, 629-648, https://doi.org/10.5194/cp-13-629-2017, 2017.

Gong, H., Xiao, H., Chen, Q., and Wang L.: Impact of Internal Climate Variability on Wintertime Surface Air Temperature Trends Over Eurasia in the SM1 Large Ensemble, Journal of Geophysical Research-Atmospheres, 127, 10, e2021JD035340, https://doi.org/10.1029/2021JD035340, 2022.

Hakim, G. J., Emile-Geay, J., Steig, E. J., Noone, D., Anderson, D. M., Tardif, R., Steiger, N., and Perkins W. A.: The last millennium climate reanalysis project: Framework and first results, J. Geophys. Res. Atmos., 121, 6745-6764, https://doi.org/10.1002/2016JD024751, 2016.

Harris, I., Osborn, T. J., Jones, P., and Lister, D.: Version 4 of the CRU TS monthly high-resolution gridded multivariate climate dataset, Scientific Data, 7, 109, https://doi.org/10.1038/s41597-020-0453-3, 2020.

Hua, W., Qin, M., Dai, A., Zhou, L., Chen, H., and Zhang W.: Reconciling human and natural drivers of the tripole pattern of multidecadal summer temperature variations over Eurasia, Geophysical Research Letters, 48, 12, e2021GL093971, https://doi.org/10.1029/2021GL093971, 2021.

https://doi.org/10.5194/essd-2026-295
Preprint. Discussion started: 23 June 2026

IPCC: Climate change 2022: Summary for Policymakers. Impacts, Adaptation, and Vulnerability. Contribution of Working Group II to the Sixth Assessment Report of the Intergovernmental Panel on Climate Change, Cambridge: Cambridge University Press, 2022.

Jain, S., Scaife, A. A., Shepherd, T. G. , Deser, C., Dunstone, N., Schmidt, G. A., Trenberth, K. E. and Turkington, T.: Importance of internal variability for climate model assessment, npj Climate and Atmospheric Science, 6, 68, https://doi.org/10.1038/s41612-023-00389-0, 2023.

Jansson, F., Edeling, W., Attema, J., and CrommelinD.: Assessing uncertainties from physical parameters and modelling choices in an atmospheric large eddy simulation model, Philos Trans A Math Phys Eng Sci, 379, 2197, 20200073, https://doi.org/10.1098/rsta.2020.0073, 2021.

Karl, T. R., Arguez, A., Huang, B., Lawrimore, J. H., McMahon, J. R., Menne, M. J., Peterson, T. C. Vose, R. S. and Zhang H. M.: Possible artifacts of data biases in the recent global surface warming hiatus, Science, 348, 6242, 1469-1472, https://www.science.org/doi/10.1126/science.aaa5632, 2015.

Lorenz, E. N.: Atmospheric Predictability as Revealed by Naturally Occurring Analogues. J. Atmos. Sci., 26, 636-646, https://doi.org/10.1175/1520-0469(1969)26<636:APARBN>2.0.CO;2, 1969.

Lorenz, E. N.: Empirical orthogonal functions and statistical weather prediction, Scientific Report No. 1, Massachusetts Institute of Technology, Department of Meteorology, 1956.

Luterbacher, J., Liniger M. A., Menzel, A., Estrella, N., Della-Marta, P. M., Pfister, C., Rutishauser, T., and Xoplaki, E.: Exceptional European warmth of autumn 2006 and winter 2007: Historical context, the underlying dynamics, and its phenological impacts, Geophysical Research Letters, 34, L12704, https://doi.org/10.1029/2007GL029951, 2007.

Man, W., Zhou, T., and Jungclaus, J. H.: Simulation of the East Asian Summer Monsoon during the Last Millennium with the MPI Earth System Model, Journal of Climate, 25, 22, 7852-7866, https://doi.org/10.1175/JCLI-D-11-00462.1, 2012.

Marotzke, J., and Forster, P. Forcing, feedback and internal variability in global temperature trends, Nature, 517, 565-570, https://doi.org/10.1038/nature14117, 2015.

Medhaug, I., Stolpe, M. B., Fischer, E. M., and Knutti, R.: Reconciling controversies about the 'global warming hiatus', Nature, 545, 7652, 41-47, https://doi.org/10.1038/nature22315, 2017.

Muggeo, V. M. R.: Estimating regression models with unknown break-points, Statist. Med., 22, 3055-3071, https://doi.org/10.1002/sim.1545, 2003.

Neukom, R., Steiger, N., Gómez-Navarro, J. J., Wang, J., and Werner, J. P: No evidence for globally coherent warm and cold periods over the preindustrial Common Era. Nature, 571, 7766, 550-554, https://doi.org/10.1038/s41586-019-1401-2, 2019.

North, G. R., Bell, T. L., Cahalan, R. F., and Moeng, F. J.: Sampling Errors in the Estimation of Empirical Orthogonal Functions, Monthly Weather Review, 110, 7, 699-706, https://doi.org/10.1175/1520-0493(1982)110<0699:SEITEO>2.0.CO;2, 1982.

https://doi.org/10.5194/essd-2026-295
Preprint. Discussion started: 23 June 2026

Pfister, L., Brönnimann, S., Schwander, M., Isotta, F. A., Horton, p., and Rohr, C.: Statistical reconstruction of daily precipitation and temperature fields in Switzerland back to 1864, Climate of the Past, 16, 663-678, https://doi.org/10.5194/cp-16-663-2020, 2020.

Po-Chedley, S., Fasullo, J. T., Siler, N., Labe, Z. M., Barnes, E. A., Bonfils, C. J. W., and Santer, B. D.: Internal variability and forcing influence model-satellite differences in the rate of tropical tropospheric warming, Proc. Natl. Acad. Sci. U.S.A., 119, 47, e2209431119, https://doi.org/10.1073/pnas.2209431119, 2022.

Ren, G., Chan, J. C. L., Kubota, H., Zhang, Z., Li, J., Zhang, Y., Zhang, Y., Yang, Y., Ren, Y., Sun, X., Su, Y., Liu, Y., Hao, Z., Xue, X., and Qin, Y.: Historical and recent change in extreme climate over East Asia, Climatic change, 168, 3-4, 22, https://doi.org/10.1007/s10584-021-03227-5, 2021.

Santer, B. D., Wigley, T. M. L., Boyle, J. S., Gaffen, D. J., Hnilo, J. J., Nychka, D., Parker, D. E., and Taylor, K. E.: Statistical significance of trends and trend differences in layer-average atmospheric temperature time series, J. Geophys. Res., 105, D6, 7337-7356, https://doi.org/10.1029/1999JD901105Digital Object Identifier, 2000.

Shi, F., Ge, Q. S., Yang, B., Li, J., Yang, F., Ljungqvist, F. C., Solomina, O., Nakatsuka, T., Wang, N., Zhao, S., Xu, C., Fang, K., Sano, M., Chu, G., Fan, Z., Gaire, N. P., and Zafar M. U.: A multi-proxy reconstruction of spatial and temporal variations in Asian summer temperatures over the last millennium, Climatic Change, 131, 4, 663-676, https://doi.org/10.1007/s10584-015-1413-3, 2015.

Smerdon, J. E., Kaplan, A., Chang, D., and Evans, M. N.: A Pseudoproxy Evaluation of the CCA and RegEM Methods for Reconstructing Climate Fields of the Last Millennium, Journal of Climate, 24, 4856-4880, https://doi.org/10.1175/2010JCLI3328.1, 2010.

Steiger, N. J., Hakim, G. J., Steig, E. J., Battisti, D. S., and Roe, G. H.: Assimilation of Time-Averaged Pseudoproxies for Climate Reconstruction, Journal of Climate, 27, 1, 426-441, https://doi.org/10.1175/JCLI-D-12-00693.1, 2014.

von Storch, H., Cubasch, U., Gonzalez-Rouco, J. F., Jones J. M., Voss R., Widmann M., and Zorita E.: Combining paleoclimatic evidence and GCMs by means of Data Assimilation Through Upscaling and Nudging (DATUN), In: Proceedings of the 11th Symposium on Global Change Studies, American Meteorological Society, Long Beach, CA, USA, 28-31, 2000.

von Storch, H., Zorita, E., Jones, J. M., Dimitriev, Y., González-Rouco, F., and Tett, S. F.: Reconstructing past climate from noisy data. Science (New York, N.Y.), 306, 5696, 679-682, https://www.science.org/doi/10.1126/science.1096109, 2004.

Wang, F., Arseneault, D., Boucher, E., Gennaretti, F., Lapointe, F., Yu, S., and Francus, P.: Volcanic Imprints in Last-Millennium Land Summer Temperatures in the Circum-North Atlantic Area, Journal of Climate, 36, 17, 5923-5939, https://doi.org/10.1175/JCLI-D-23-0107.1, 2023.

Wang, Y., Le, T. H., Chen, G., Yung, Y. L., Su, H., Seinfeld, J. H., and Jiang J. H.: Reduced European aerosol emissions suppress winter extremes over northern Eurasia, Nature Climate Change, 10, 3, 225-230, https://doi.org/10.1038/s41558-020-0693-4, 2020.

https://doi.org/10.5194/essd-2026-295
Preprint. Discussion started: 23 June 2026

Yan, X., Zhang, X., and Zhong, L.: A gridded temperature reconstruction for East Asia during 1400-2000 CE [Data set], Zenodo, https://doi.org/10.5281/zenodo.18477496, 2026.

Yang, K., Hua, W., and Hu, Q.: A multi-model analysis of the East Asian monsoon changes in the Medieval Climate Anomaly and Little Ice Age, Int J Climatol, 40, 5084-5097, https://doi.org/10.1002/joc.6506, 2020.

Yiou, P., Boichu, M., Vautard, R., Vrac, M., Jourdain, S., Garnier, E., Fluteau, F., and Menut, L.: Ensemble meteorological reconstruction using circulation analogues of 1781-1785, Climate of the Past, 10, 2, 797-809, https://doi.org/10.5194/cp-10-797-2014, 2014.

Yun, S., Smerdon, J. E., Li, B., and Zhang X.: A pseudoproxy assessment of why climate field reconstruction methods perform the way they do in time and space, Climate of the Past, 17, 2583-2605, https://doi.org/10.5194/cp-17-2583-2021, 2021.

Zhang, H., Li, M. and Hu, Y.: Paleoclimate data assimilation: Principles and prospects, Sci. China Earth Sci., 68, 407-424, https://doi.org/10.1007/s11430-024-1439-y, 2025a.

Zhang, H., Werner, J. P., García-Bustamante, E., González-Rouco, F., Wagner, S., Zorita, E., Fraedrich, K., Jungclaus, J. H., Ljungqvist, F. C., Zhu, X., Xoplaki, E., Chen, F., Duan, J., Ge, Q., Zhixin Hao, Ivanov, M., Schneider, L., Talento, S., Wang, J., Yang B., and Luterbacher, J.: East Asian warm season temperature variations over the past two millennia, Scientific Reports, 8, 7702, https://doi.org/10.1038/s41598-018-26038-8, 2018.

Zhang, L.: The roles of external forcing and natural variability in global warming hiatuses, Climate Dynamics, 47, 9-10, 3157-3169, https://doi.org/10.1007/s00382-016-3018-6, 2016.

Zhang, X., Yan, X., Wu, M., and Zheng J.: The Examination of an Improved Analogue Method for Gridded Temperature Variation Reconstruction, International Journal of Climatology, 45, e8755, https://doi.org/10.1002/joc.8755, 2025b.

Zorita, E., and H. von Storch, H.: The Analog Method as a Simple Statistical Downscaling Technique: Comparison with More Complicated Methods. J. Climate, 12, 2474-2489, https://doi.org/10.1175/1520-0442(1999)012<2474:TAMAAS>2.0.CO;2, 1999.